Journal of Materials Chemistry A

PAPER

View Article Online
View Journal | View Issue

Cite this: J. Mater. Chem. A, 2018, 6, 1714

Carbon-supported metal nanodendrites as efficient, stable catalysts for the oxygen reduction reaction†

Luna B. Venarusso, [a] Chirley V. Boone, [a] Jefferson Bettini [b] and Gilberto Maia *[a]

The search for efficient, stable electrocatalysts for the oxygen reduction reaction (ORR) has received increased attention, given the need to speed up this reaction in fuel cells. This article reports the one-pot synthesis of novel metal nanodendrites (MNDs) of Pt or Pt–Pd alloy surface-covering patterns that, supported on Vulcan Carbon XC-72, effectively catalyzed the ORR. The surface of Vulcan Carbon XC-72 exhibits raised plains interspersed with ribbed troughs, in a pattern energetically favorable to metal precipitation (deposition) into the ribbed troughs. This produces MND/C structures that are strongly catalytic toward the ORR. Mass-specific activity (MSA) of 0.56 mA μg^{-1} and specific activity (SA) in the 1.17–1.35 mA cm^{-2} range are noteworthy findings for Pt/C, Pt@Au′/C, and Pt–Pd/C MND electrocatalysts at 0.9 $V_{iR\text{-free}}$, using platinum-group metal (PGM) loadings as low as 26 $\mu g\ cm^{-2}$—better values, therefore, than the United States Department of Energy (DOE) targets for MSA (0.44 A mg_{Pt}^{-1}) and SA (0.72 mA cm^{-2} at 0.9 $V_{iR\text{-free}}$) for electrocatalysts used in portable applications to be marketed in 2017, and for cathode areal PGM loadings (<50 $\mu g_{PGM}\ cm^{-2}$), as well as better than the commercial E-Tek Pt/C (20% Pt mass) catalyst.

Received 12th October 2017
Accepted 29th December 2017

DOI: 10.1039/c7ta08964c

rsc.li/materials-a

1. Introduction

Three major obstacles, not strictly mutually independent, need to be overcome before fuel cells can attain full commercial viability:[1] the high cost of Pt, the slow kinetics of the oxygen reduction reaction (ORR)—five-or-more orders of magnitude slower than the hydrogen oxidation reaction, for Pt-based catalysts[2–5]—and the low durability of catalysts.

High Pt loadings, of at least 0.4 mg cm^{-2}, have been required at the cathode for fuel cells to achieve desirable performance,[6–8] prompting extensive research into mitigating this requirement by improving the intrinsic activity of Pt-based electrocatalysts for the ORR without compromising fuel cell performance.[9] This has been achieved using Pt-alloy-based electrocatalysts enriched with one or more elements capable of altering the availability of active surface sites (the ensemble effect) or the binding strength of reactants, intermediates, products, and spectator species (the electronic and/or strain effect), offering catalytic performance[9] comparable to that of pure Pt in terms of mass-specific activity (MSA), as well as developing durable Pt-based electrocatalysts with a huge range of compositions.[1]

Pt-Alloy catalysts are typically deposited onto carbon black powder (Vulcan XC 72 or XC 72R), the support material most often employed to prepare electrocatalysts for low-temperature fuel cell applications.[10] Carbon black particles exhibit a large specific surface area, facilitating dispersion of active components, are low cost, widely available,[11] and have good electric conductivity and a porous structure.[9]

A common experimental procedure to produce carbon-supported Pt alloys is the colloidal/chemical precipitation method, which involves a metal salt, the carbon support, and a capping agent to be mixed into the aqueous solution, followed by reduction of metal ions to the metallic state by addition of an aqueous solution of a reducing agent.[9–11] The capping agent controls the size of Pt-alloy particles and prevents them from agglomerating. Production of Pt-alloy nanoparticles depends on experimental conditions such as pH, reaction temperature, type of solvent and reducing agents employed.[9]

During long-term operation of fuel cells, oxidation of the carbon support to CO_2 ($C + 2H_2O \rightarrow CO_2 + 4H^+ + 4e^-$) is catalyzed by the presence of Pt, a process that may cause sintering or agglomeration of Pt-alloy nanoparticles (Pt may also be lost from the electrode—separation of Pt particles from the carbon surface[11]—by transport of Pt ions through the liquid, ionomer, or both), decreasing the electrocatalytic surface area, degrading

[a]Institute of Chemistry, Universidade Federal de Mato Grosso do Sul, Av. Senador Filinto Muller, 1555, Campo Grande, MS 79074-460, Brazil. E-mail: gilberto.maia@ufms.br; Fax: +55 67 3345 3552; Tel: +55 67 3345 3551

[b]Brazilian Nanotechnology National Laboratory (LNNano), Rua Giuseppe Máximo Scolfaro, 10000, Campinas, SP 13083-100, Brazil

† Electronic supplementary information (ESI) available: The supporting information contains figures, equations, and tables concerning supplementary results, and references. See DOI: 10.1039/c7ta08964c

the catalyst, and thus decreasing fuel cell performance.[9] Degradation of this carbon-based system can also result from a lack of chemical interaction between Pt particles and the carbon support—a lack that can be mitigated by depositing Pt in the presence (or absence) of Pd on the Au–carbon support, since Au provides high electrical conductivity[12] and better chemical interaction with the support.

Examples of good catalysts for the ORR are trimetallic PtNiCo octahedra on carbon black (PtNiCo/C), octahedral PtNi/C,[13] hexapod-like ternary PtNiCo alloy nanostructures,[14] dendritic PtCuNi cubes[15] (the last two initially obtained as metal nanoparticles, followed by exposure to Vulcan XC-72), Pd_1Pt_5 dendrites with preferential exposure of {1 1 1} facets supported on Vulcan XC-72 carbon,[16] carbon-supported Pt-based icosahedral nanocages with surfaces enclosed both by {1 1 1} facets and by twin boundaries,[17] Pd@$Pt_{2.7}$L/C catalyst,[18] Pd@Pt–Ni/C with octahedral core–shell nanocrystals,[19] Pd–Pt polycrystalline alloy (PdPt/C alloy), Pd@Pt/C core–shell,[20] Pd_3Au@Pt/C (superthin platinum shell less than 1 nm thick),[21] and rhombic dodecahedral bimetallic AuPt@Pt nanocrystals with dendritic branches (loaded on a carbon support after nanoparticle synthesis).[22] Changes in Pt d-band properties have been reported when this metal is coupled with Pd in nanocrystals, also resulting in a mismatch between Pt and Pd lattice constants.[23] Bimetallic Pt-enriched Pt–Pd alloys have shown improved activity toward the ORR.[24–28]

Theoretical studies of formulations combining Pt, Pd, and Au have suggested that PtPdAu thin films can be improved with the use of small, controlled amounts of Au, which retard the dissolution of under-coordinated Pt atoms[29] (Au-conferred resistance to formation of Pd–OH and Pt–OH bonds in $Pd_9Au_1/Pt_{monolayer}$ nanoparticles under ORR conditions, experimentally improving the stability of these particles[30,31]) and enhancing the activity of ternary PtPdAu systems toward the ORR,[32,33] with potential application in proton-exchange membrane fuel cells.[29]

The novel contribution of the present investigation lies in its use of a one-pot method to synthesize novel metal nanodendrites (MNDs) supported on Vulcan Carbon XC-72 (MND/Cs) (nanocomposites synthesized from metal precursors in the presence of Vulcan Carbon XC-72, differently from our previous approach,[32] which yielded porous metallic nanostars in the absence of Vulcan Carbon XC-72, but no porous nanostars in the presence of this carbon black powder), which exhibited high electrocatalytic activity toward the ORR, using less than 50 μg_{PGM} cm^{-2} (PGM: platinum-group metal) for cathode areal loading (in our previous publication,[32] a PGM amount of 85 μg_{PGM} cm^{-2} was employed, accounting for a total metal (Pt and/or Pd, and/or Au) amount of 152.7 μg cm^{-2}, in comparison with a maximum total metal amount of 53 μg cm^{-2} in the present investigation)—the United States Department of Energy (DOE) target for 2020.[34] Mono-, bi-, and trimetallic nanoparticles were synthesized employing Pt, Pd, Au, and Ni precursors. Electrochemically active surface areas and surface compositions were estimated by cyclic voltammetry (CV). Electrocatalytic activity and durability of the new materials were evaluated by hydrodynamic cyclic voltammetry (HCV) using rotating ring-disc electrodes. MND/C morphologies, compositions, and structures were characterized by physical methods (TEM, HRTEM, XRD, HAADF-STEM, electron diffraction patterns, thermogravimetry, and energy-dispersive X-ray (EDX) microanalysis).

An apparently major disadvantage of using catalysts containing three precious metals (Pt, Au, and Pd) would be cost (US\$5.012 $\times$ 10^{-5}, US\$5.012 $\times$ 10^{-5}, and $\sim$US\$2.0 $\times$ 10^{-5} per microgram, respectively[35]), but we will demonstrate that the commercial cost of Pt-based catalysts is at least 2.5 times higher than our novel catalysts. Additional disadvantages of Pt-based catalysts during the operation of fuel cells include poor stability of Pt (resulting in dissolution, sintering, and agglomeration,[2,36] none of which appear to occur with our catalysts, as will be shown), possible competing reduction reactions,[36] and poisoning of the active sites owing to methanol crossover[2,36] (when this alcohol is involved).

2. Experimental

2.1. Materials and methods

$PdCl_2$, $NiCl_2 \cdot 6H_2O$, K_2PtCl_6, $CuSO_4 \cdot 5H_2O$, ascorbic acid (AA), acetone (all Vetec), $HAuCl_4 \cdot 3H_2O$, Pt (10 wt%) on carbon (both Sigma-Aldrich), Pluronic F-127, Nafion 20 wt% (both Aldrich), Vulcan Carbon XC-72 (C) (Cabot), and E-Tek Pt/C (20% Pt mass) were the salts, precursor solutions, and solvents employed.

A three-electrode glass cell with a working electrode (Pine Research Instrumentation) consisting of a Teflon-embedded glassy-carbon-disk/Au(or Pt)-ring rotating assembly (0.196 and 0.11 cm^2 geometric areas, respectively), with a collection efficiency of $N = 0.26$, was employed for the voltammetric measurements. The counter-electrode was a Pt plate (Degussa) and the reference electrode was a reversible hydrogen electrode (RHE).

2.2. Electrode preparation

The working glassy carbon (GC) disk electrode was initially polished with 2500-grit emery paper and alumina slurries (1 and 0.05 μm) and sequentially cleaned by sonication in Milli-Q water (Millipore), acetone, and 0.1 M $HClO_4$ (Tedia) solution, for 5 min in each solvent. The Au (or Pt) ring underwent 200 cycles at 900 mV s^{-1} in the 0.05–1.7 V (or 0.05–1.2 V, for the Pt ring) potential range (changing the solution whenever necessary to ensure a clean surface finish). A uniform thin film was then generated by dripping 30 μL of a 1 mg mL^{-1} aqueous solution of MND/Cs (loading: 152.7 μg cm^{-2}) onto a GC disk surface, which was allowed to dry at room temperature. An additional step of dripping 5 μL of Nafion (0.01%) onto a modified GC disk surface was performed, followed by drying at room temperature. The resulting modified electrodes were placed in an electrochemical cell containing a 0.1 M aqueous solution of $HClO_4$ subsequently saturated with N_2 (5.0 purity) or O_2 (4.0 purity) (both from Air Liquide).

2.3. Sample preparation for TEM, HRTEM, and EDX measurements

Diluted MND/C aqueous solutions were dripped onto ultrathin carbon films supported on lacey carbon film on 400-mesh

copper grids (Ted Pella), for use in the TEM, HRTEM, and EDX experiments. For EDX measurements, MND/C aqueous solutions dripped onto fluorine-doped tin oxide (FTO)-coated glass slides (0.5 cm × 0.5 cm × 0.2 cm, Flexitec, $R_{\square} = 11\ \Omega\ \square^{-1}$) (loading: 152.7 μg cm^{-2}) were used.

2.4. Apparatuses and measurements

CV and HCV, the electrochemical techniques employed, were run on an AFP2 WaveDriver 20 bipotentiostat–galvanostat (Pine Research Instrumentation) coupled to an AFMSRCE modulated-speed rotator.

A PGSTAT128N potentiostat/galvanostat (Autolab) equipped with a FRA2.X module was used in the electrochemical impedance spectroscopy (EIS) experiments, conducted at a fixed potential—namely, at an open-circuit potential of around 1.04 V (on average) in the presence of a 0.1 M aqueous solution of $HClO_4$, with potential perturbation of 25 mV (rms) within a frequency range of 10 mHz to 100 kHz. Care was taken (as described in ref. 37) to ensure that AC impedance data corresponded to the interfaces being investigated at high frequencies. Each HCV curve was corrected for ohmic-drop resistance measured and calculated from the fitted high-frequency intercept determined using EIS. The ohmic-drop resistance measured in 0.1 M $HClO_4$ averaged 30 Ω.

MND/C nanostructures were characterized by TEM, performed on a JEM 2100F apparatus (Jeol) equipped with a scanning transmission electron microscope (STEM) and an EDX detector (Thermo Noran System) operating at 200 kV or on a Philips CM200 apparatus operating at 200 kV. An EDX system (Thermo Noran System Six) was used to determine the metallic atomic compositions, which were reported to represent an average of three measurements of the same sample. Structural phase identification of the synthesized MND/C samples was investigated employing powder XRD *via* a Siemens D5000 X-ray diffractometer (plus Diffrac Plus XRD Commander software) using Cu Kα radiation ($\lambda = 0.154$ nm), at a scan rate of 0.02° s^{-1} for 2θ.

TG characterizations of C, Pluronic F-127, and MND/Cs were performed using a TGA-50 thermogravimetric analyzer (Shimadzu) on 2–5 mg samples under a Synthetic Air 5.0 FID gas flow (50 mL min^{-1}) at temperatures ranging from ambient to 900 °C and a heating rate of 10 °C min^{-1}, using alumina crucibles.

Normalization of cyclic voltammograms was based on electrochemically active surface area (ECSA) values, by integrating charges in the desorption region of underpotential deposition (upd) of the hydrogen monolayer (H_{upd} stripping)[38] (50 mV s^{-1}) and stripping in the desorption region of the copper monolayer upd (Cu_{upd}).[28,38,39] Charge density was taken as 210 μC cm^{-2} (ref. 40) for desorption of a hydrogen monolayer from the MND surface, 420 μC cm^{-2} (ref. 38 and 39) for reduction of a copper monolayer covering the MND surface, and 400 μC cm^{-2} for the reduction of an oxygen monolayer covering the Au surface.[40] Cu_{upd}-stripping was performed by anodic dissolution voltammetry in a 0.1 M $HClO_4$ solution containing 1 mM $CuSO_4$. The potentials at the electrodes modified with MND/Cs supported on glassy carbon (MND/C/GCs) were initially kept at 1.0 V for 200 s to avoid copper deposition onto these electrodes, followed by a 900 s step at 0.3 V for deposition of a copper monolayer and subsequently by a linear hydrodynamic voltammetry sweep from 0.3 to 1.0 V at 5 mV s^{-1} and 600 rpm.

2.5. MND/C synthesis

MND/Cs were prepared using a one-pot method. Pt/C MNDs were synthesized in a small beaker with 9 mL of an aqueous solution at 80 °C containing 16 mg of Vulcan Carbon XC-72, 10 mg of K_2PtCl_6 (corresponding to a final 20% mass of pure Pt in the Pt/C MND) and 11.4 mg of Pluronic F-127 (used as a structure-directing agent for MNDs[32,41]). A 1 mL volume of an aqueous solution containing 17 mg of AA was quickly added under stirring. The resulting solution was then stirred for 2 h at 80 °C. Synthesis of other mono-, bi-, and trimetallic nanoparticles was performed using Pt, Pd, Au, and Ni precursors (see details in Table 1).[32,41]

Preparation of Pt–Pd@Au′/C MNDs, for instance, included 2.35 mg of $PdCl_2$, 5.12 mg of $HAuCl_4 \cdot 3H_2O$, and 3.10 mg of $NiCl_2 \cdot 6H_2O$, in addition to Vulcan Carbon XC-72 and Pt salt (Table 1). Employing AA amounts 4.45 times greater (in mmol) than those of salt precursor proved necessary to guarantee metal nanoparticle production.[32] MNDs synthesized in the presence of Ni^{2+} (here identified by names containing an apostrophe) were obtained through reactions carried out under stirring in an N_2 atmosphere.[32] Ni^{2+} is not reduced by AA.[32]

MND/Cs were isolated by centrifuging at 4500 rpm for 30 min, where the residual Pluronic F-127 was removed at 2 h of reaction, followed by ten consecutive cycles of centrifugation and washing with Milli-Q water, and finally by drying at 40 °C. For further characterization, the MND/Cs thus collected were redispersed in water under sonication to produce an ink-like suspension.

3. Results and discussion

3.1. MND/C characterization

The TEM images revealed 10 to 50 nm-long MND structures (dark pieces) distributed on Vulcan Carbon XC-72 (light gray "fingerprint" areas). The structures constituted 2 to 5 nm-long Pt or Pt–Pd alloy nanodendrites (Fig. 1 and 2). (The alloy assumption will be subsequently expanded.) Generation of metallic structures as MNDs was attributed to the Vulcan Carbon XC-72 support, since a similar synthesis procedure performed in the absence of this support material resulted in porous nanostars.[32] XRD patterns (Fig. 3) and, as shown later, electron diffraction images, revealed these MND/Cs to have fcc crystalline patterns with (1 1 1), (2 0 0), (2 2 0), (3 1 1), and (2 2 2) main planes.

Crucial at this point is explaining how the MND structures are formed on the Vulcan Carbon XC-72 support. Visible in Fig. 1 are light gray fingerprint-like areas resembling flakes, making up a noteworthy surface constituted of raised plains interspersed with ribbed troughs, in a pattern energetically favorable to the precipitation (deposition) of metals into the

Table 1 Salt and element masses, salt amounts of substance, Pluronic F-127 masses, and ascorbic acid (AA) masses and volumes in the solution used to synthesize metal nanodendrites supported on Vulcan Carbon XC-72 (MND/C)

MND/C	Mass (mg) and amount of substance (mmol)	Element mass (mg)	Pluronic F-127 mass (mg)	AA mass (mg) and volume (mL) in the solution
Pt/C	C: 16 and 1.34 K_2PtCl_6: 10 and 0.021	C: 16 Pt: 4	11.4	17 and 1
Pt′/C	C: 16 and 1.34 K_2PtCl_6: 10 and 0.021 $NiCl_2 \cdot 6H_2O$: 3.10 and 0.013	C: 16 Pt: 4 Ni: 0.8	18.7	27.7 and 1.63
Pt–Pd/C	C: 16 and 1.34 K_2PtCl_6: 10 and 0.021 $PdCl_2$: 2.35 and 0.013	C: 16 Pt: 4 Ni: 1.4	18.7	27.7 and 1.63
Pt@Au/C	C: 16 and 1.34 K_2PtCl_6: 10 and 0.021 $HAuCl_4 \cdot 3H_2O$: 5.12 and 0.013	C: 16 Pt: 4 Au: 2.6	18.7	27.7 and 1.63
Pt–Pd′/C	C: 16 and 1.34 K_2PtCl_6: 10 and 0.021 $PdCl_2$: 2.35 and 0.013 $NiCl_2 \cdot 6H_2O$: 3.10 and 0.013	C: 16 Pt: 4 Pd: 1.4 Ni: 0.8	26.0	38.4 and 2.26
Pt–Pd@Au/C	C: 16 and 1.34 K_2PtCl_6: 10 and 0.021 $PdCl_2$: 2.35 and 0.013 $HAuCl_4 \cdot 3H_2O$: 5.12 and 0.013	C: 16 Pt: 4 Pd: 1.4 Au: 2.6	26.0	38.4 and 2.26
Pt@Au′/C	C: 16 and 1.34 K_2PtCl_6: 10 and 0.021 $HAuCl_4 \cdot 3H_2O$: 5.12 and 0.013 $NiCl_2 \cdot 6H_2O$: 3.10 and 0.013	C: 16 Pt: 4 Au: 2.6 Ni: 0.8	26.0	38.4 and 2.26
Pt–Pd@Au′/C	C: 16 and 1.34 K_2PtCl_6: 10 and 0.021 $PdCl_2$: 2.35 and 0.013 $HAuCl_4 \cdot 3H_2O$: 5.12 and 0.013 $NiCl_2 \cdot 6H_2O$: 3.10 and 0.013	C: 16 Pt: 4 Pd: 1.4 Au: 2.6 Ni: 0.8	33.3	49.1 and 2.90

ribbed troughs. This results in nanodendrite-like structures electrocatalytically very active toward the ORR, as will be described.

Fig. 2 shows the most representative HRTEM images of the synthesized MND/Cs. Clearly discernible fringe patterns are observed for the MND/C structures, with a crystalline pattern (0.226 nm for Pt/C (Fig. 2A) and Pt–Pd/C (Fig. 2B)—red lines represent distances characteristic of Pt and Pt–Pd alloy crystalline patterns[28,33,42]) and a number of stepped edges (the MND/Cs structures) (Fig. 2). For Pt@Au′/C (Fig. 2C) and Pt–Pd@Au′/C (Fig. 2D), a 0.226–0.231 nm crystalline pattern was found (red lines represent distances characteristic of Pt and Pt–Pd alloy upon a core of Au crystalline patterns[28]).

The XRD patterns of Pt/C, Pt–Pd/C, Pt@Au′/C, and Pt–Pd@Au′/C (Fig. 3) exhibit peaks characteristic of face-centered cubic (fcc) crystalline Pt, Pd, and Au, with diffraction peaks at $2\theta = 40°$, 46°, 67.6°, 82°, and 85.6° for Pt and Pd planes (1 1 1), (2 0 0), (2 2 0), (3 1 1), and (2 2 2), respectively, identified for Pt/C and Pt–Pd/C (PDF# 652868 (Pt) and PDF# 894897 (Pd), respectively), in addition to peaks at $2\theta = 38.8°$, 44.8°, 65.2°, 77.2°, and 80.8°, identified for Pt@Au′/C and Pt–Pd@Au′/C (PDF# 040784 (Au))—all values in agreement with ref. 33. No diffraction peaks corresponding to fcc crystalline Ni (PDF# 701849) were identified. The broad peak exhibiting the highest 2θ value, of 24.3–25.2°, corresponding to a (0 0 2) plane, is indicative of the graphitic state[43] of the C-supported samples.

Formation of a Pt–Pd alloy is evident, since the presence of Pd did not alter the XRD patterns from Pt/C to Pt–Pd/C. In Pt@Au′/C, however, Au is not alloyed with Pt, as shown by the fact that XRD peaks characteristic of Au and Pt appear clearly separated, reinforcing the assumption of formation of a Au core with a Pt shell. For Pt–Pd@Au′/C, the XRD peaks for Au and the Pt–Pd alloy are clearly dissociated (Fig. 3), suggesting production of a Au core with a Pt–Pd alloy shell.

Applying Scherrer's equation—$L = 0.90\ \lambda/(\beta_{1/2} \cos \theta)$,[44,45] where L is the average crystallite size, λ is the X-ray wavelength (1.5418 Å), $\beta_{1/2}$ is the diffraction peak width at half height in radians, and θ is the angle, with the last two at maximum peak position (1 1 1)[28]—yielded L values of 3.8 (Pt/C), 5.3 (Pt–Pd/C), 2.6 (Pt@Au′/C), and 3.1 nm (Pt–Pd@Au′/C), in agreement with the observed sizes of C-supported metallic nanodendrites (Fig. 1 and 2). A noteworthy feature is that crystal structures are constituted of 2 to 5 nm-long Pt or Pt–Pd alloy nanodendrites, while the TEM images (Fig. 1) revealed 10 to 50 nm-long metal particles distributed on Vulcan Carbon XC-72. We attributed this difference to the insufficient contribution of nanodendrites

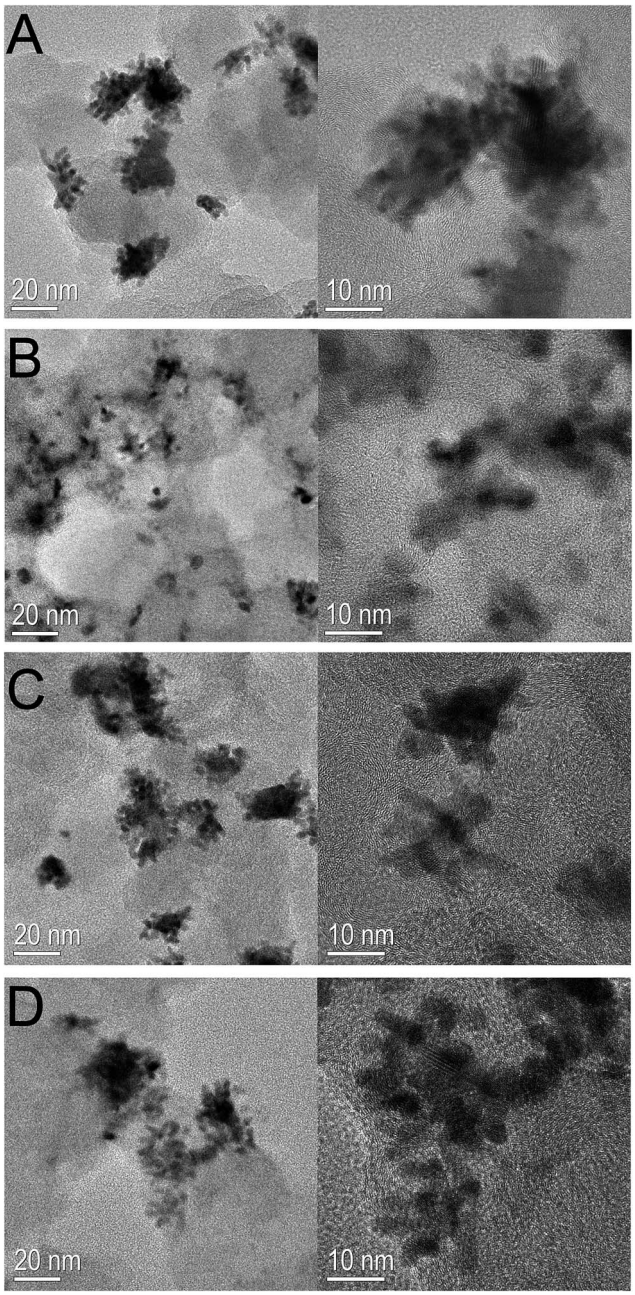

Fig. 1 Representative TEM images of the synthesized MND/Cs. (A) Pt/C; (B) Pt–Pd/C; (C) Pt@Au′/C; (D) Pt–Pd@Au′/C.

to the generation of packed metal particles, in the present case. When the nanodendrites are more packed in the metal particles, the crystal structures are larger, even though these particles have similar sizes, as shown in the TEM images (8 to 10 nm *vs.* up to 50 nm-long on average;[28] 20 to 40 nm *vs.* 80 nm-long on average[33]).

Unit cell size (a)[28,45] was calculated as 0.39 nm for Pt/C and Pt–Pd/C and as 0.4015 nm for Pt@Au′/C and Pt–Pd@Au′/C, values similar to those of bulk Pt (PDF# 652868, $a = 0.3924$ nm) and higher than those of bulk Pd (PDF# 89489, $a = 0.389$ nm), suggesting formation of a Pt–Pd alloy, and virtually identical to the value for bulk Au (PDF# 040784, $a = 0.4078$ nm), suggesting an absence of Au in the alloy. Spacings between crystal planes (d)[28,45] were calculated as 0.225 nm for Pt/C and Pt–Pd/C and as 0.232 nm for Pt@Au′/C and Pt–Pd@Au′/C, in entire agreement with the spacing between planes observed in the HRTEM images (Fig. 2).

The EDX mapping images (Fig. 4) revealed that the MNDs in Pt–Pd@Au′/C had a thin Pt–Pd alloy surface layer of Pt–Pd alloy nanodendrites covering a base comprising metallic Au nanostructures, while for MNDs in Pt@Au′/C a thin surface layer of Pt nanodendrites covers a base constituted by metallic Au nanostructures. In alloy structures (Pt–Pd/C), metals are assumed to form randomly distributed metal–metal bonds.[46] The EDX mapping images showed MNDs to have a base constituted by metallic Au nanostructures that suggest Au, Pd, and Pt depositions with temporal separations, initially yielding a Au core, followed by a nanodendritic nanoporous Pt–Pd alloy or Pt outer shell.[32,41] Au nanoparticles most probably serve as *in situ* seeds for subsequent deposition of the Pt–Pd alloy or Pt outer shell.[32,41]

Pluronic F-127 oriented growth of the nanodendritic Pt–Pd alloy or the Pt outer shell.[32,41] During Pt–Pd or Pt deposition, Pluronic F-127 chains were adsorbed onto the Pt–Pd or Pt surface with their hydrophobic poly(propylene oxide) (PPO) groups, forming cavities that facilitated formation of the dendritic Pt–Pd alloy or the Pt outer shell.[32,41]

The EDX mapping images corroborate the EDX mass percentages shown in Table S1 (ESI†) regarding the absence of detection of metallic Ni in MNDs synthesized in the presence of Ni^{2+} (Pt′/C, Pt–Pd′/C, Pt@Au′/C, Pt–Pd@Au′/C). Ma *et al.*[47] proposed that Ni^{2+} can mediate facet evolution during the generation of structures by deposited Ni (the Ni underpotential deposition layer will be galvanically replaced by $[PtCl_6]^{2-}$ precursor and Pt^{II} intermediate species during synthesis). This can be the case with the present study, since the ORR electrocatalytic responses barely differ for MND/Cs synthesized in the absence or presence of Ni^{2+} (Fig. 1 and 2; Table S2, ESI†).

TG analysis (Fig. S1, ESI†) showed that Vulcan Carbon XC-72 burned effectively at 610 °C and completely at 700 °C (100% mass loss). Pluronic F-127 burns effectively at 256 °C and almost completely at 370 °C (96% mass loss). TG responses for MND/Cs revealed small mass losses (2–4%) in the 145–270 °C range, possibly related to burning of residual Pluronic F-127 left on MND/C surfaces even after several runs of centrifugation and washing in Milli-Q water. MND/Cs burned effectively at 350 °C (~529 °C for Pt@Au/C), with ~65–81% mass loss at ~518 °C (~67% mass loss at ~642 °C for Pt@Au/C). Pt@Au/C and Pt@Au′/C burned at much higher temperatures than the other MND/Cs, suggesting that the nanodendritic nanoporous Pt–Pd alloy (in the presence or absence of Au) or pure Pt contribute more effectively to MND/C burning. When serving as support for metallic nanoparticles, C burns more effectively (roughly 58–182 °C lower) than bare C.

TG measurements showing that metal content in MND/Cs was 27.3 wt% on average (Table S1, ESI†) were combined with EDS measurements for weight percentages of metals, revealing final C and metal contents in the nanocomposites to be very similar to pre-synthesis compositions (Table S1, ESI†). The

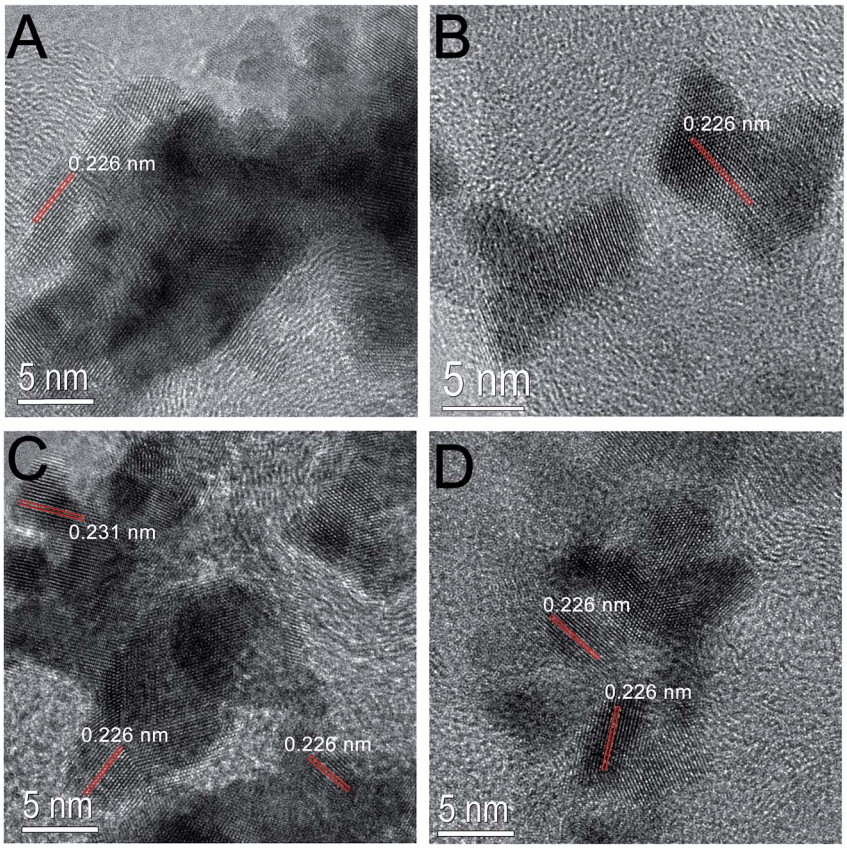

Fig. 2 Representative HRTEM images of the synthesized MND/Cs. (A) Pt/C; (B) Pt–Pd/C; (C) Pt@Au′/C; (D) Pt–Pd@Au′/C.

exception was metallic Ni, not detected after synthesis (Table S1, ESI†).

3.2. Electrochemical profile

Fig. 5 shows the CV responses obtained with MND/C-modified GC disk electrodes in 0.1 M $HClO_4$ saturated with N_2, at a scan rate of 50 mV s^{-1} between 0.05 and 1.2 V (Fig. S2, ESI,† shows the CV response obtained with a GC disk electrode modified with E-Tek Pt/C (20% Pt mass)). The voltammograms exhibit characteristic features of a polycrystalline Pt electrode with regard to the hydrogen and oxygen adsorption/desorption regions, whether in positive- or negative-going scans.[32,33] The double-layer[48,49] charging/discharging region (compare the CV curves for bare GC and GC modified with Vulcan Carbon XC-72 in Fig. S2, ESI†) is slightly enlarged because of the presence of Vulcan Carbon XC-72 in the MND/Cs. Fig. 5B shows typical resolved peaks (expansion of Fig. 5A) in the hydrogen desorption region (0.05–0.40 V), which are associated with strongly bonded hydrogen species on different crystal faces of metallic Pt.[50] These responses were similar to those obtained for Pt (1 1 1)[51] and tetrahedral Pt[52] in 0.1 M $HClO_4$. The small oxidation peaks observed between 0.10 and 0.27 V (Fig. 5A and B) can be assigned to (1 1 0) sites and the step contribution associated with (1 0 0)/(1 1 1) terrace sites,[52] respectively.

In Pt–Pd/C and Pt–Pd′/C, however, the electrochemical responses differed slightly from those of other nanocomposites in the hydrogen desorption region, as shown by the green and cyan curves, respectively, in Fig. 5C (which expands Fig. 5A). The typical peaks of the hydrogen desorption region disappeared and a broad peak is visible, owing to the presence of Pd (Pt–Pd alloy) on the surface.[50,51] The presence of Au cores in Pt–Pd@Au/C and Pt–Pd@Au′/C (magenta and gray curves, respectively; Fig. 5C) facilitates formation of peaks typical of the Pt hydrogen desorption region, as observed in Fig. 5B, suggesting that Pd is slightly less exposed at the surface of these nanocomposites. Also, the CV responses depicted in Fig. S3 (ESI†) suggest complete coverage of the Au core surface during MND/C synthesis, as previously shown in Fig. 5.

For Pd-containing catalysts, a cautious approach is necessary when calculating ECSA values, given the presence of hydrogen species absorbed into the metallic Pd structure,[53] which can considerably alter ECSA values obtained through H_{upd} stripping. For this reason, Cu_{upd}-stripping was employed.[28,38,39] Fig. 6 shows the hydrodynamic cyclic and linear voltammograms of the electrodes modified with Pd-containing MND/Cs (Pt–Pd/C, Pt–Pd′/C, Pt–Pd@Au/C, and Pt–Pd@Au′/C) in the absence and presence of 1 mM $CuSO_4$ (black and red curves, respectively).

The black curves in Fig. 6 behave similarly to those depicted in Fig. 5. However, the red curves in Fig. 6 show clearly visible peaks at low and high potentials that can be attributed to removal of Cu deposited at Pd and Pt sites,[39] respectively, on the MND surface.

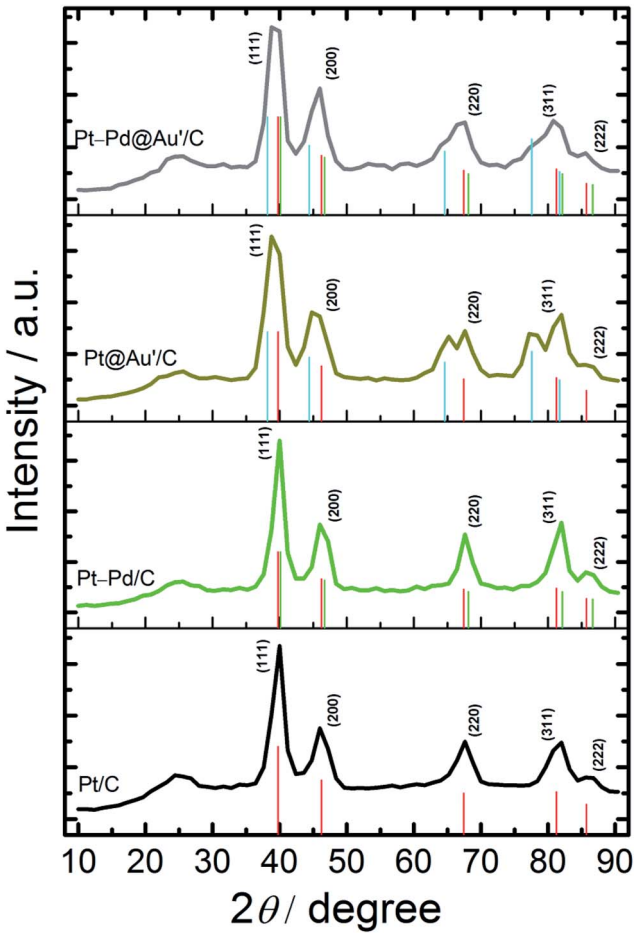

Fig. 3 XRD patterns of Pt/C, Pt–Pd/C, Pt@Au′/C, and Pt–Pd@Au′/C. Vertical lines correspond to PDF# 652868 (Pt, red), PDF# 894897 (Pd, green), and PDF# 040784 (Au, cyan).

Using charge densities of H_{upd} electrodesorption to determine ECSAs may not be a reliable approach, given the significant percentage of corner and edge atoms in Pt nanoparticles.[54] In addition, for electrodes composed of highly dispersed Pt- and Pd-based nanoparticles, ECSA values obtained by the Cu_{upd}-stripping method are assumed to be more accurate.[38,55] Furthermore, Cu_{upd}-stripping is an even more robust method for metal alloy nanoparticles.[56]

ECSA values calculated from H_{upd}- and Cu_{upd}-stripping for MND/Cs were virtually identical (Fig. S4, ESI†), demonstrating that hydrogen and copper adsorption can take place at the same sites, irrespective of alloy type or MND shape.

3.3. Evaluation of the electrocatalytic activity of modified MND/C/GC electrodes toward the ORR

The electrocatalytic activity toward oxygen reduction was examined *via* HCV measurements made in O_2-saturated 0.1 M $HClO_4$, subtracting the background curves read for each modified electrode in N_2-saturated 0.1 M $HClO_4$, and finally correcting for ohmic-drop resistance. Fig. 7A shows the HCVs obtained with a GC disk electrode modified with MND/Cs at an electrode rotation rate of 1600 rpm (Fig. S5A, ESI,† shows the HCV curves obtained with a GC disk electrode modified with E-Tek Pt/C (20% Pt mass)). Current densities were calculated per geometric area of a bare GC electrode. MND/Cs and E-Tek Pt/C (20% Pt mass) showed diffusion-limited current densities (j_d)—the j_d theoretical value (Levich equation[57]) expected for HCV at 1600 rpm is close to -5.8 mA cm^{-2}, and experimental values oscillating up to 10% around the theoretical value, as was the case with the present results, are considered appropriate, indicating sufficient loading of metal catalysts.[23,58] For the Pt(10 wt%)-on-carbon/GC electrode, j_d was much lower than the theoretical value expected (Fig. S5B, ESI†) for the ORR in the 0.05–0.75 V potential region, with diffusional and kinetic current density contributions observed at 0.75–1.05 V. Above 1.05 V, current densities approach zero (the region of complete oxygen coverage of the Pt or Pt–Pd surface, with oxide formation). The difference between forward and back scans is roughly 60 mV more negative in terms of potential for the back scan in the diffusional and kinetic current density region.

$E_{1/2}$ values (the potential at $1/2j_d$; Fig. 7A) for MND/C/GC electrodes ranged from 0.91 (Pt–Pd′/C and Pt–Pd@Au/C) to 0.93 V (Pt@Au′/C) in the forward scan. An $E_{1/2}$ value of 0.89 V was found for E-Tek Pt/C (20% Pt mass) in the forward scan (Table S2, ESI†). The inset to Fig. 7A provides an overview of $E_{1/2}$ values.

High specific activity (SA) values, of 1.17 mA cm^{-2} for Pt/C and Pt–Pd/C, and high MSA values, of 0.53–0.56 mA μg^{-1} for Pt/C and Pt@Au′/C, were found at 0.9 $V_{iR\text{-free}}$ (Fig. 7B and Table S2, ESI;† see also eqn (S1) and (S2), ESI,† employed to calculate SA and MSA, respectively), which are much better values than those obtained for E-Tek Pt/C (20% Pt mass) (SA = 0.29 mA cm^{-2} and MSA = 0.13 mA μg^{-1}; Table S2, ESI†). These values meet the DOE targets of 0.44 A mg_{Pt}^{-1} for MSA and 0.72 mA cm^{-2} at 0.9 $V_{iR\text{-free}}$ for SA for electrocatalysts used in portable applications to be marketed in 2017,[36] as well as some of the targets reported previously[13–21,28,32,33] (Table S2, ESI†).

Also, the low PGM loadings of 26–41 μg cm^{-2} (less than 50 μg_{PGM} cm^{-2} for cathode areal loading, the 2020 DOE target[34]) employed for the MND/Cs investigated in the present study resulted in specific ECSA values of 29–65 m^2 g^{-1} (see Table S2, ESI;† see also eqn (S3), ESI,† employed to calculate specific ECSA). For E-Tek Pt/C (20% Pt mass), PGM loading was 31 μg cm^{-2} and ECSA was 46 m^2 g^{-1} (Table S2, ESI†). The high loading of precious metals involved in the Pt–Pd@Au/C MND/C catalyst, with a combined cost of roughly US$0.0016 for a joint 37 μg of Pt, Au, and Pd[35] (see Tables S1 and S2, ESI†), added to around US$0.0008 for synthesizing the catalyst (including the cost of Vulcan Carbon XC-72), results in a total of US$0.0024 for 153 μg of Pt–Pd@Au/C MND/Cs—lower, however, by a factor of 2.5, than the cost of commercial Pt-based catalysts (US$0.0060 for 153 μg of Pt/C (20% Pt mass) under the best purchasing conditions).

For GC electrodes modified with MND/Cs or E-Tek Pt/C (20% Pt mass), the corresponding ring current densities at a bare Au or Pt ring electrode maintained at 1.2 V (Fig. S6 and S7, ESI†) and coupled with disk HCVs (Fig. 7A; S5, ESI†) were practically negligible in the case of bare Au, but improved for the bare Pt ring, indicating that, even for the latter, minimal amounts of

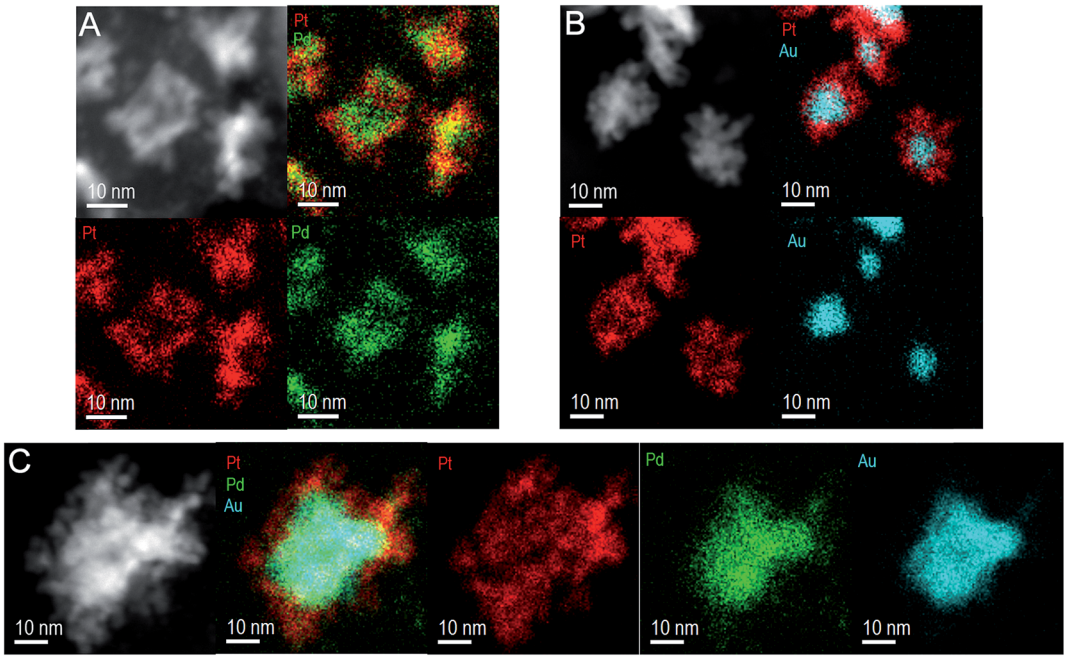

Fig. 4 Representative EDX mapping images for (A) Pt–Pd/C, (B) Pt@Au′/C, and (C) Pt–Pd@Au′/C.

peroxide intermediates were generated during the ORR. This demonstrates the high efficiency of MND/Cs (or E-Tek Pt/C (20% Pt mass)) as electrocatalysts toward this reaction, with water as the final product. The idea of using a bare Au ring instead of a bare Pt ring drew on the assertion, by Zhou *et al.*,[59] that the oxidation of a Pt surface has a strong effect on H_2O_2 oxidation, since the processes taking place on the Pt surface are not mass-transfer-limited (instead, the rate of electrochemical H_2O_2 oxidation on Pt is limited by internal electron transfer between H_2O_2 and $Pt(OH)_2$ (ref. 59)). No oxidation occurs below 1.2 V on the surface of a Au ring biased at this potential.[59] However, Zhou *et al.*,[59] also found that the current of H_2O_2 oxidation on a Au ring is even lower than that observed on Pt. The calculated percentages of H_2O_2 ranged from 0.3% (Pt–Pd@Au/C) to 1% (Pt@Au′/C) at 0.12 V (the potential at the disk MND/C/GC electrodes) in the forward scans (see eqn (S4) and (S5), ESI,† used to calculate $X_{H_2O_2}$, the percentage of H_2O_2 formation) using a bare Au ring, and varied from 0.3% to 4.2% for Pt@Au′/C (the best H_2O_2 producer among the MND/C/GC electrodes investigated) at 0.12 V. For the same potential and direction scan, the E-Tek Pt/C (20% Pt mass)/GC electrode provided H_2O_2 generation rates of 0.6% and 4.2%, obtained using bare Au and Pt rings, respectively.

The mechanism of action of MND/Cs and E-Tek Pt/C (20% Pt mass) toward the ORR was evaluated *via* hydrodynamic voltammetries conducted at varying rotation rates (Fig. S8, ESI†).

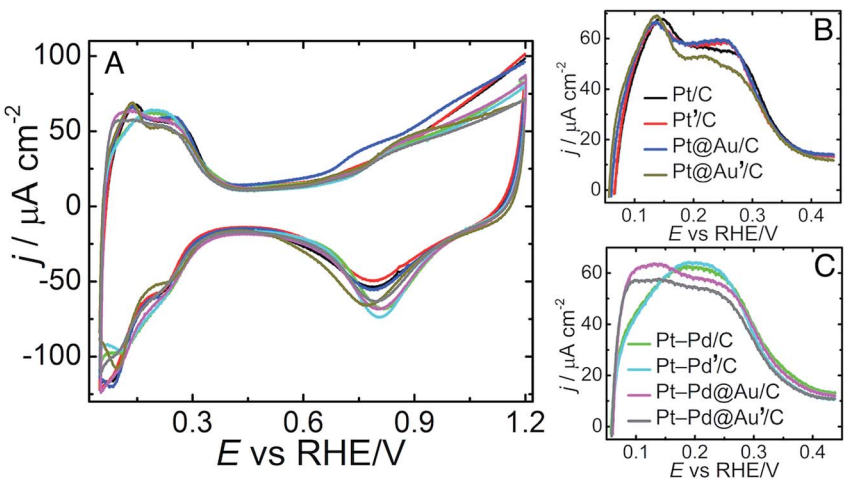

Fig. 5 (A) Cyclic voltammograms of a GC electrode modified with MND/Cs recorded in N_2-saturated 0.1 M $HClO_4$. Scan rate: 50 mV s^{-1}. Scans started at 1.2 V. (B and C) Hydrogen desorption region expanded from the curves in (A).

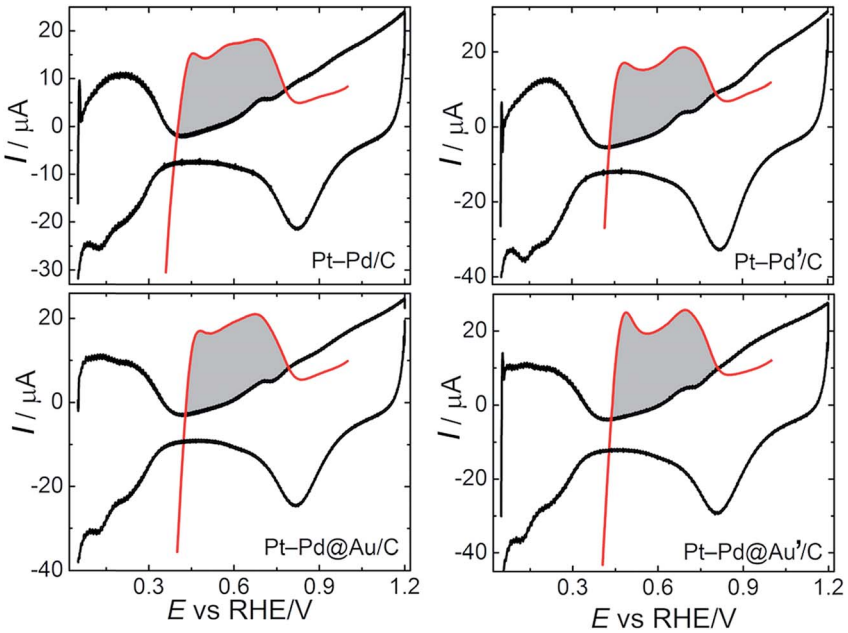

Fig. 6 Hydrodynamic cyclic voltammograms recorded with GC electrodes modified with Pt–Pd/C, Pt–Pd′/C, Pt–Pd@Au/C, and Pt–Pd@Au′/C nanocomposites in N_2-saturated 0.1 M $HClO_4$ in the 0.05–1.2 V potential range (black curves; scans started at 0.05 V). The hydrodynamic linear voltammograms overlap and were obtained in a N_2-saturated 0.1 M $HClO_4$ solution containing 1 mM $CuSO_4$, in the 0.3–1 V potential range (red curves; scans started at 0.3 V). $\omega = 600$ rpm, ν: 5 mV s^{-1}. The gray areas were used to determine ECSAs based on Cu_{upd}-stripping.[28,38,39]

Based on the linear behavior exhibited by a Koutecký–Levich[57] plot (Fig. S6A and S7C and eqn (S6), ESI†) obtained at two potentials (0.3 V (for E-Tek Pt/C (20% Pt mass) alone) and 0.9 V) and the corresponding slope values, an n value of 4.0 was determined for both MND/Cs and E-Tek Pt/C (20% Pt mass) (Table S3, ESI†). These results, in conjunction with the very small generation of H_2O_2 (a maximum of 4.2% for Pt@Au′/C), suggest the principal mechanism to be direct production of H_2O involving four electrons ($O_2 + 4H^+ + 4e^- \rightarrow H_2O$). The Tafel plot (Fig. S6B and S7D, ESI†) exhibits two well-defined linear regions with slopes approaching the expected values of −60 and −120 mV dec^{-1} for low- and high-current regions, respectively (Table S3, ESI†), reported to occur during the ORR on Pt[4,5,32,33,60] and Pd surfaces.[4,5,32,33,61] The first charge-transfer step is a rate-determining factor in both current regions, and, depending on the current region, this step involves adsorption of reaction intermediates.[60]

3.4. Electrocatalytic stability test

Pt/C, Pt@Au′/C, and Pt–Pd@Au′/C MND were tested for stability in O_2-saturated 0.1 M $HClO_4$ at a potential scan rate of 50 mV s^{-1} for 10 000 cycles between 0.6 and 1.0 V.[32,33] The HCV readings obtained before (black curves) and after (red curves) testing are depicted in Fig. 8 and in Fig. S9 (ESI†). For Pt/C (solid curves), the limiting current decreased by only 0.88%, but $E_{1/2}$ remained unchanged. Similar behaviors were observed for GC electrodes modified with Pt@Au′/C and Pt–Pd@Au′/C (Fig. S9, ESI†).

After the stability test, TEM images revealed no perceptible changes in the structures of MND/Cs (insets to Fig. 8 and S10, ESI†). Also, the nanostructures retained their uniform distribution on the support, without agglomerating or forming larger nanocrystals.

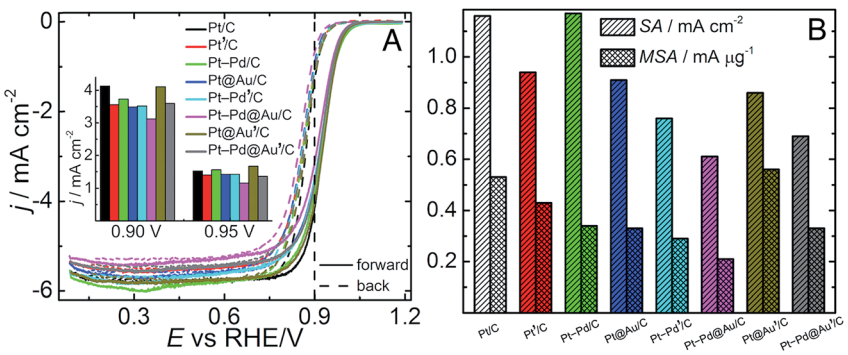

Fig. 7 (A) Hydrodynamic cyclic voltammograms for GC electrodes modified with MND/Cs in O_2-saturated 0.1 M $HClO_4$. $\omega = 1600$ rpm; scan rate: 10 mV s^{-1}. Scans started at 0.05 V. Inset: j values at 0.9 and 0.95 V for the forward scan. (B) SA and MSA values at 0.90 V.

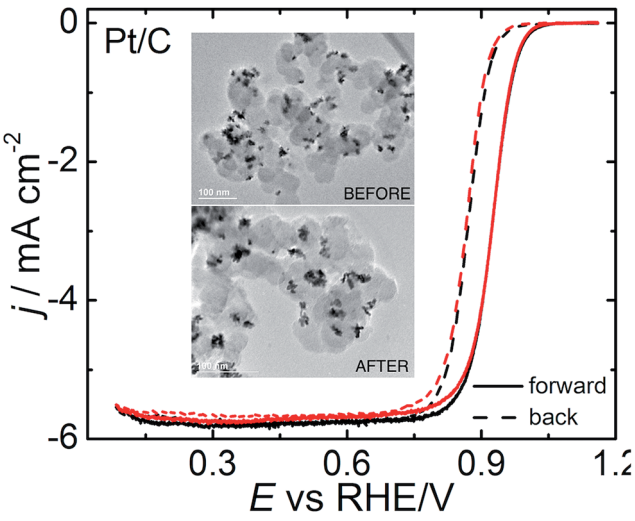

Fig. 8 Hydrodynamic cyclic voltammograms for GC electrodes modified with the Pt/C electrocatalyst before and after the stability test (10 000 cycles between 0.6 and 1.0 V at 50 mV s^{-1}) in O_2-saturated 0.1 M $HClO_4$. ω = 1600 rpm; scan rate: 10 mV s^{-1}. Scans started at 0.05 V. Inset: representative TEM images of Pt/C before and after 10 000 potential scans.

The decreased ECSA and specific ECSA values (Table S2, ESI†) observed after the stability test can be explained by Ostwald ripening[32,33,62,63]—*i.e.*, dissolution and redeposition of Pt or Pt–Pd nanodendrites at MND edges.[32,33,62,63] Superficial nanodendrites appeared smoothed after 10 000 potential scans (insets to Fig. 8 and 9; S9, ESI†), but without deleterious effects on MSA (0.53 mA μg^{-1} for Pt/C and Pt@Au′/C at 0.90 $V_{iR\text{-free}}$ (Table S2, ESI†) after 10 000 potential scans). After 10 000 potential scans, the SA values of Pt/C, Pt@Au′/C, and Pt–Pd@Au′/C MND/Cs rose to 1.19, 1.35, and 0.82 mA cm^{-2}, respectively, at 0.90 $V_{iR\text{-free}}$ (Table S2, ESI†). These values meet the DOE targets of 0.44 A mg_{Pt}^{-1} for MSA and 0.72 mA cm^{-2} at 0.9 $V_{iR\text{-free}}$ for SA for electrocatalysts used in portable applications to be marketed in 2017.[36]

The TEM images in Fig. 8, 9, and S9 (ESI†) clearly reveal that metals settle (and remain stable) in the energetically favorable region—*i.e.*, the ribbed troughs on the surface of Vulcan Carbon XC-72, resulting in nanodendrite-like structures that prove electrocatalytically very active even after the stability test.

Representative TEM and electron diffraction pattern images obtained before and after 10 000 potential scans (Fig. 9) revealed preservation of MND distribution and nanodendritic Pt or Pt–Pd alloy covering patterns (compare TEM and HRTEM images in Fig. 1 and 8). As shown by electron diffraction patterns, crystallinity was also preserved after the stability test.

Diffraction images (Fig. 9) of Pt/C obtained before and after 10 000 potential scans show an fcc crystalline pattern corresponding to the Pt [0 1 1] zone axis, with (1 1 1), (2 2 0), and (3 1 1) main planes at distances of 0.228 nm (in total agreement with the distance obtained from the HRTEM image (Fig. 2A) and XRD pattern (Fig. 3)), 0.141 nm, and 0.117 nm, respectively. For Pt@Au′/C, an fcc crystalline pattern with distances corresponding to (1 1 1), (2 2 0), and (3 1 1) planes typical of Pt and Au materials can be observed, while for Pt–Pd@Au′/C the diffraction patterns correspond to the [0 1 1] zone axis, with (1 1 1), (2 2 0), and (3 1 1) main planes and varying distances between Pt, Pd, and Au planes. Pt–Pd alloy nanodendrites located at the edges are oriented toward and attached to the Au surface.

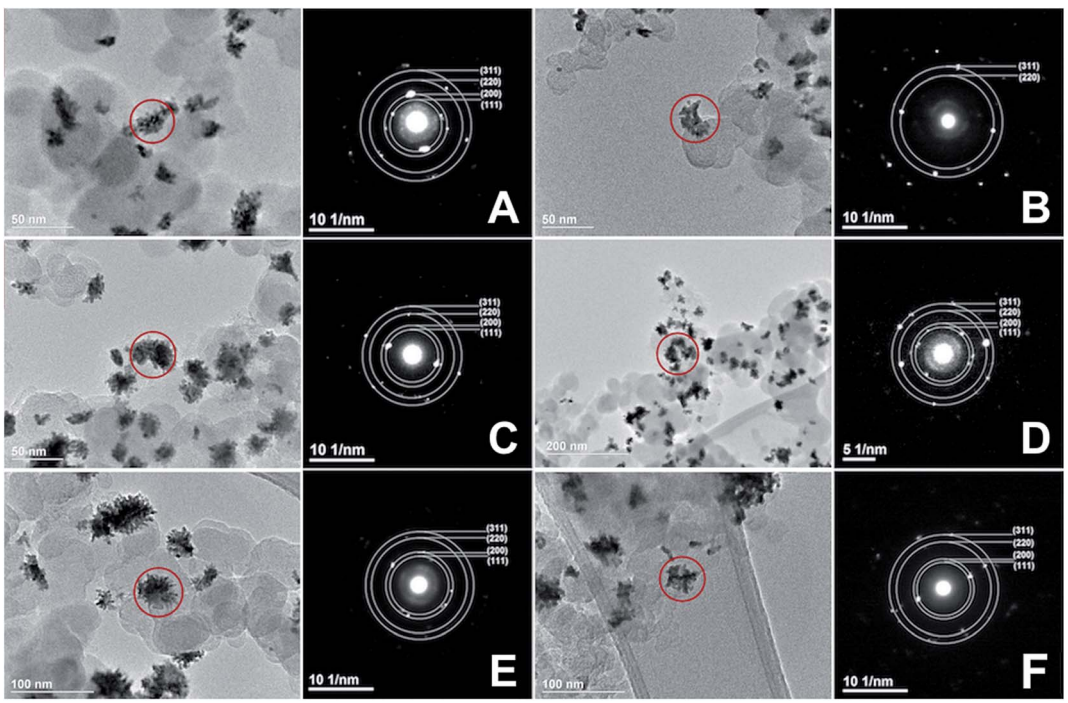

Fig. 9 Representative TEM images and electron diffraction patterns of (A) Pt/C, (B) Pt/C after 10 000 cycles, (C) Pt@Au′/C, (D) Pt@Au′/C after 10 000 cycles, (E) Pt–Pd@Au′/C, and (F) Pt–Pd@Au′/C after 10 000 cycles.

EDX mapping images were also recorded after 10 000 potential scans (Fig. S10, ESI†). The stability test for catalytic activity caused no pronounced changes to the MNDs. No dissolution of inner metallic nanoparticles, such as Au, were detected (see EDX mapping in Fig. S10, ESI†).

A number of noteworthy features account for the excellent electrocatalytic activity—relative to DOE targets—and stability of MND/Cs:

(1) the strong bond between MNDs and Vulcan Carbon XC-72 (see TEM and HRTEM images in Fig. 1, 2, 8, and 9, and S9, ESI;† for TG responses, see Fig. S1, ESI†), as well as large specific surface area, low cost, good electric conductivity, and porous structure of Vulcan Carbon XC-72, further favoring the electric conductivity of MND/Cs, particularly because metals settle (and remain stable) where the energy on Vulcan Carbon XC-72 surface is minimal—*i.e.*, the ribbed troughs.

(2) MND structures comprised a thin surface layer of porous nanodendrites of Pt or Pt–Pd alloy (see XRD patterns in Fig. 3)—MNDs contain a large percentage of corner and edge atoms—exhibiting an fcc crystalline pattern (see TEM and HRTEM images in Fig. 1, 2, 8, and 9, and S9, ESI;† see also EDX mapping images in Fig. 4 and S10, ESI,† as well as electron diffraction images in Fig. 9). Changes in Pt d-band properties have been reported when this metal is coupled with Pd in nanocrystals, also resulting in a mismatch between Pt and Pd lattice constants.[23] Bimetallic Pt-enriched Pt–Pd alloys have shown improved activity toward the ORR.[24–28]

(3) the presence of Pd on the surface of the Pt–Pd alloy (Fig. 4 and 5) (random metal–metal bonds at the atomic level) contributes to decreasing the adsorption energy of oxygen[64] and/or intermediates involved in the ORR, as may also occur with the thin Pt layer on the Au core of MNDs. It is suggested that the ORR performance of PtPdAu ternary systems can be improved[32,33] using a small, controlled amount of Au, which retards the dissolution of under-coordinated Pt atoms[29] (Au-conferred resistance to formation of Pd–OH and Pt–OH bonds in $Pd_9Au_1/Pt_{monolayer}$ nanoparticles under ORR conditions[30,31]).

(4) no perceptible changes occurred in the MND/C structures, whose uniform distribution on the support was preserved, without agglomeration or formation of larger nanocrystals after the stability tests (Fig. 8; S9, ESI†). This also suggests an absence of oxidation of the carbon support, in addition to preservation of MND distribution and nanodendritic Pt or Pt–Pd alloy covering patterns (compare TEM images in Fig. 1 and 8) and crystallinity (see electron diffraction patterns in Fig. 9). Also, when Pt and/or Pd are deposited onto carbon-supported Au, this metal provides better chemical interaction with the support, minimizing or precluding carbon degradation.

Together, these features account for the excellent electrocatalytic activity—relative to DOE targets—and stability of the MND/C catalysts investigated, particularly Pt/C, Pt′/C, Pt–Pd/C, and Pt@Au′/C. Also noteworthy is that even though the high loading of precious metals (a total 37 μg of Pt, Au, and Pd in the Pt–Pd@Au/C MND/C catalyst) has a combined cost of roughly US$0.0016 for these precious metals[35] (see Tables S1 and S2, ESI†), in addition to approximately US$0.0008 to synthesize the catalyst (including the cost of Vulcan Carbon XC-72 support), the estimated total cost to produce 153 μg of Pt–Pd@Au/C MND/Cs will be just US$0.0024—lower therefore, by a factor of 2.5, than the cost of Pt-based commercial catalysts (*e.g.*, US$0.0060 for 153 μg of Pt/C (20% Pt mass)).

4. Conclusions

The novel Vulcan Carbon XC-72-supported MND structures ranged in size from 10 to 50 nm, exhibited fcc crystalline patterns, contained large percentages of corner and edge atoms, were constituted by a thin surface layer of porous nanodendrites (2–5 nm) of Pt or Pt–Pd alloy (with presence of Pd on the surface of the alloy), and effectively catalyzed the ORR, with high performance in terms of MSA (0.53–0.56 mA μg^{-2}) and SA (1.16–1.35 mA cm^{-2}) at 0.9 $V_{iR\text{-free}}$ for Pt/C, Pt′/C, Pt–Pd/C, and Pt@Au′/C, much better values than for E-Tek Pt/C (20% Pt mass). The combination of Pd and Pt in nanocrystals changes Pt d-band properties, owing to Pd coupling, also resulting in a mismatch between Pt and Pd lattice constants. In PtPdAu ternary systems, Au may provide resistance to formation of Pd–OH and Pt–OH bonds, both of which improve catalytic activity toward the ORR. Combined with low PGM loadings (26–41 μg cm^{-2}), which met DOE targets set for 2017–2020, these features suggest the utility of these MNDs for use in acid fuel cells, in addition to an MND/C production cost that is lower, by a factor of 2.5, than that of commercial Pt-based catalysts, even when three precious metals are employed. Furthermore, ECSA and specific ECSA values of 2.0–3.3 cm^2 and 29–65 $m^2\ g^{-1}$, respectively, were obtained, with high $E_{1/2}$ values (0.91–0.93 V). After the stability test, no changes were perceived in the structures of the novel electrocatalysts, which retained a uniform distribution on the support, without agglomerating or forming larger nanocrystals, suggesting an absence of oxidation of the carbon support, in some cases aided by the superior chemical interaction between Au and carbon support. Also, the stability test had no deleterious effect on MND distribution, nanodendritic Pt or Pt–Pd alloy covering pattern, or crystallinity. All these relevant conclusions can be directly attributed to the Vulcan Carbon XC-72 surface pattern of raised plains interspersed with ribbed troughs, the latter of which are far more energetically favorable sites for metal precipitation (deposition), resulting in MND/C structures that prove strongly catalytic toward the ORR.

Conflicts of interest

The authors declare no competing financial interests.

Acknowledgements

The authors wish to thank LNNano and LME-IQ-Unesp for the TEM facilities and GFQM-IQ-Unesp for the XRD facilities. Thanks are also given to CNPq (grants 301403/2011-2, 473991/2012-8, 405695/2013-6, 303759/2014-3, and 442268/2014-9) and Fundect-MS (grants 23/200.583/2012, 23/200.735/2012, 23/200.246/2014, and 59/300.184/2016) for their financial support. L. B. V. and C. V. B thank CAPES for the fellowship.

References

1 X. Huang, Z. Zhao, L. Cao, Y. Chen, E. Zhu, Z. Lin, M. Li, A. Yan, A. Zettl, Y. M. Wang, X. Duan, T. Mueller and Y. Huang, *Science*, 2015, **348**, 1230.

2 W. Xia, A. Mahmood, Z. Liang, R. Zou and S. Guo, *Angew. Chem., Int. Ed.*, 2015, **55**, 2650.

3 M. K. Debe, *Nature*, 2012, **486**, 43.

4 G. V. Fortunato, L. B. Venarusso and G. Maia, *ChemElectroChem*, 2014, **1**, 625.

5 L. B. Venarusso, R. H. Sato, P. A. Fiorito and G. Maia, *J. Phys. Chem. C*, 2013, **117**, 7540.

6 Y. Nie, L. Li and Z. Wei, *Chem. Soc. Rev.*, 2015, **44**, 2168.

7 M. Shao, Q. Chang, J.-P. Dodelet and R. Chenitz, *Chem. Rev.*, 2016, **116**, 3594.

8 C. M. Pedersen, M. Escudero-Escribano, A. Velázquez-Palenzuela, L. H. Christensen, I. Chorkendorff and I. E. L. Stephens, *Electrochim. Acta*, 2015, **179**, 647.

9 Y.-J. Wang, N. Zhao, B. Fang, H. Li, X. T. Bi and H. Wang, *Chem. Rev.*, 2015, **115**, 3433.

10 Y. Holade, N. E. Sahin, K. Servat, T. W. Napporn and K. B. Kokoh, *Catalysts*, 2015, **5**, 310.

11 S. Shahgaldi and J. Hamelin, *Carbon*, 2015, **94**, 705.

12 A. Wittstock, A. Wichmann and M. Bäumer, *ACS Catal.*, 2012, **2**, 2199.

13 X. Huang, Z. Zhao, Y. Chen, E. Zhu, M. Li, X. Duan and Y. Huang, *Energy Environ. Sci.*, 2014, **7**, 2957.

14 A. Oh, Y. Jin Sa, H. Hwang, H. Baik, J. Kim, B. Kim, S. H. Joo and K. Lee, *Nanoscale*, 2016, **8**, 16379.

15 Y. Kuang, Y. Zhang, Z. Cai, G. Feng, Y. Jiang, C. Jin, J. Luo and X. Sun, *Chem. Sci.*, 2015, **6**, 7122.

16 Y. Ye, J. Joo, S. Lee and J. Lee, *J. Mater. Chem. A*, 2014, **2**, 19239.

17 X. Wang, L. F. Cosme, X. Yang, M. Luo, J. Liu, Z. Xie and Y. Xia, *Nano Lett.*, 2016, **16**, 1467.

18 X. Wang, S.-I. Choi, L. T. Roling, M. Luo, C. Ma, L. Zhang, M. Chi, J. Liu, Z. Xie, J. A. Herron, M. Mavrikakis and Y. Xia, *Nat. Commun.*, 2015, **6**, 7594.

19 X. Zhao, S. Chen, Z. Fang, J. Ding, W. Sang, Y. Wang, J. Zhao, Z. Peng and J. Zeng, *J. Am. Chem. Soc.*, 2015, **137**, 2804.

20 Y. Lim, S. K. Kim, S.-C. Lee, J. Choi, K. S. Nahm, S. J. Yoo and P. Kim, *Nanoscale*, 2014, **6**, 4038.

21 H. Li, R. Yao, D. Wang, J. He, M. Li and Y. Song, *J. Phys. Chem. C*, 2015, **119**, 4052.

22 L. Zhang, S. Yu, J. Zhang and J. Gong, *Chem. Sci.*, 2016, **7**, 3500.

23 H. Zhang, M. Jin and Y. Xia, *Chem. Soc. Rev.*, 2012, **41**, 8035.

24 L. Liu, G. Samjeske, S. Nagamatsu, O. Sekizawa, K. Nagasawa, S. Takao, Y. Imaizumi, T. Yamamoto, T. Uruga and Y. Iwasawa, *J. Phys. Chem. C*, 2012, **116**, 23453.

25 F.-M. Li, X.-Q. Gao, S.-N. Li, Y. Chen and J.-M. Lee, *NPG Asia Mater.*, 2015, **7**, 219.

26 K. Jukk, N. Kongi, K. Tammeveski, J. Solla-Gullón and J. M. Feliu, *Electrochem. Commun.*, 2015, **56**, 11.

27 K. Jukk, N. Kongi, K. Tammeveski, J. Solla-Gullón and J. M. Feliu, *ChemElectroChem*, 2017, **4**, 2547.

28 C. V. Boone and G. Maia, *Electrochim. Acta*, 2017, **247**, 19.

29 V. Tripkovic, H. A. Hansen, J. Rossmeisl and T. Vegge, *Phys. Chem. Chem. Phys.*, 2015, **17**, 11647.

30 K. Sasaki, H. Naohara, Y. Cai, Y. M. Choi, P. Liu, M. B. Vukmirovic, J. X. Wang and R. R. Adzic, *Angew. Chem., Int. Ed.*, 2010, **49**, 8602.

31 S. Guo, S. Zhang and S. Sun, *Angew. Chem., Int. Ed.*, 2013, **52**, 2.

32 L. B. Venarusso, J. Bettini and G. Maia, *ChemElectroChem*, 2016, **3**, 749.

33 L. B. Venarusso, J. Bettini and G. Maia, *J. Solid State Electrochem.*, 2016, **20**, 1753.

34 A. Kongkanand and M. F. Mathias, *J. Phys. Chem. Lett.*, 2016, **7**, 1127.

35 P. C. K. Vesborg and T. F. Jaramillo, *RSC Adv.*, 2012, **2**, 7933.

36 M. E. Scofield, H. Liu and S. S. Wong, *Chem. Soc. Rev.*, 2015, **44**, 5836.

37 L. B. Venarusso, K. Tammeveski and G. Maia, *Electrochim. Acta*, 2011, **56**, 8926.

38 D. Chen, Q. Tao, L. W. Liao, S. X. Liu, Y. X. Chen and S. Ye, *Electrocatalysis*, 2011, **2**, 207.

39 C. L. Green and A. Kucernak, *J. Phys. Chem. B*, 2002, **106**, 1036.

40 H. Angerstein-Kozlowska, in *Comprehensive Treatise of Electrochemistry*, ed. E. Yearger, J. O.' M. Bockris, B. E. Conway and S. Sarangapani, Plenum Press, New York, 1984, vol. 9, ch. 2, pp. 15–59.

41 L. Wang and Y. Yamauchi, *J. Am. Chem. Soc.*, 2010, **132**, 13636.

42 G. V. Fortunato, F. Lima and G. Maia, *J. Power Sources*, 2016, **302**, 247.

43 Y. Fan, P.-F. Liu, Z.-Y. Huang, T.-W. Jiang, K.-L. Yao and R. Han, *J. Power Sources*, 2015, **280**, 30–38.

44 J.-N. Zheng, S.-S. Li, X. Ma, F.-Y. Chen, A.-J. Wang, J.-R. Chena and J.-J. Feng, *J. Mater. Chem. A*, 2014, **2**, 8386.

45 B. D. Cullity, *Elements of X-ray Diffraction*, Addison-Wesley Publishing Company Inc., Reading, 2nd edn, 1978.

46 Y. Tang and W. Cheng, *Nanoscale*, 2015, **7**, 16151.

47 L. Ma, C. Wang, B. Y. Xia, K. Mao, J. He, X. Wu, Y. Xiong and X. W. Lou, *Angew. Chem., Int. Ed.*, 2015, **54**, 5666.

48 B. E. Conway, *Electrochemical supercapacitors – Scientific fundamentals and technological applications*, Kluwer Academic/Plenum Publisher, New York, 1999.

49 J. R. Miller, R. A. Outlaw and B. C. Holloway, *Science*, 2010, **329**, 1637.

50 H. Li, G. Sun, N. Li, S. Sun, D. Su and Q. Xin, *J. Phys. Chem. C*, 2007, **111**, 5605.

51 R. Devivaraprasad, R. Ramesh, N. Naresh, T. Kar, R. K. Singh and M. Neergat, *Langmuir*, 2014, **30**, 8995.

52 F. J. Vidal-Iglesias, R. M. Arán-Ais, J. Solla-Gullón, E. Herrero and J. M. Feliu, *ACS Catal.*, 2012, **2**, 901.

53 M. Grdeń, M. Łukaszewski, G. Jerkiewicz and A. Czerwiński, *Electrochim. Acta*, 2008, **53**, 7583.

54 G. Jerkiewicz, *Electrocatalysis*, 2010, **1**, 179.

55 M. Shao, J. H. Odell, S.-I. Choi and Y. Xia, *Electrochem. Commun.*, 2013, **31**, 46.

56 M. Łukaszewski, M. Soszko and A. Czerwiński, *Int. J. Electrochem. Sci.*, 2016, **11**, 4442.

57 A. J. Bard and L. R. Faulkner, in *Electrochemical Methods: Fundamentals and Applications*, John Wiley & Sons, New York, 2001.
58 K. J. J. Mayrhofer, D. Strmcnik, B. B. Blizanac, V. Stamenkovic, M. Arenz and N. M. Markovic, *Electrochim. Acta*, 2008, **53**, 3181.
59 R. Zhou, Y. Zheng, M. Jaroniec and S.-Z. Qiao, *ACS Catal.*, 2016, **6**, 4720.
60 D. B. Sepa, M. V. Vojnovic and A. Damjanovic, *Electrochim. Acta*, 1981, **26**, 781.
61 L. M. Vracar, D. B. Sepa and A. Damjanovic, *J. Electrochem. Soc.*, 1986, **133**, 1835.
62 Y. Xu, M. Shao, M. Mavrikakis and R. R. Adzic, in *Fuel Cell Catalysis: A Surface Science Approach*, ed. M. T. M. Koper, Wiley, New Jersey, 2009, ch. 9, pp. 271–315.
63 K. Sasaki, M. Shao and R. Adzic, in *Polymer Electrolyte Fuel Cell Durability*, ed. F. N. Büchi, M. Inaba and T. J. Schmidt, Springer, New York, 2009, pp. 7–27.
64 L. M. C. Pinto and G. Maia, *J. Phys. Chem. C*, 2015, **119**, 8213.